Applied Catalysis B: Environmental 324 (2023) 122259

Contents lists available at ScienceDirect

Applied Catalysis B: Environmental

journal homepage: www.elsevier.com/locate/apcatb

# Anchoring Pt-doped PdO nanoparticles on γ-$Al_2O_3$ with highly dispersed La sites to create a methane oxidation catalyst

Zhi Liu [a], Guangyan Xu [a], Lingyou Zeng [e], Wei Shi [a], Yingjie Wang [d], Yanwei Sun [d], Yunbo Yu [a,b,c,d,*], Hong He [a,b,c,d,*]

[a] State Key Joint Laboratory of Environment Simulation and Pollution Control, Research Center for Eco-Environmental Sciences, Chinese Academy of Sciences, Beijing 100085, China
[b] University of Chinese Academy of Sciences, Beijing 100049, China
[c] Center for Excellence in Regional Atmospheric Environment and Key Laboratory of Urban Pollutant Conversion, Institute of Urban Environment, Chinese Academy of Sciences, Xiamen 361021, China
[d] Ganjiang Innovation Academy, Chinese Academy of Sciences, Ganzhou 341119, China
[e] School of Materials Science and Engineering, Peking University, Beijing 100871, China

ARTICLE INFO

*Keywords:*
Methane oxidation
Stability
Palladium oxides
Platinum doping
Lanthanum anchoring

ABSTRACT

Catalysts for the complete oxidation of methane suffer from poor physical and chemical stability regarding their noble metal active sites. Herein, we prepared a PtPd-$La_1/Al_2O_3$ catalyst by loading highly dispersed La species and Pt-PdO nanoparticles on γ-$Al_2O_3$ support, exhibiting significantly enhanced hydrothermal and long-term stability under the harsh conditions of simulated natural gas vehicle (NGV) exhaust. Over PtPd-$La_1/Al_2O_3$, PdO nanoparticles (NPs) can be anchored by highly dispersed La sites through electron transfer from La to PdO, inhibiting the sintering of Pd species during hydrothermal aging. Pt uniformly doped in PdO creates high-efficiency Pt sites and unsaturated Pd sites (as well as Pd sites adjacent to O defects) for water-resistance, further enhancing long-term stability. Thus, this work provides the potential to resolve tough challenges related to methane emission control on NGVs.

## 1. Introduction

Methane ($CH_4$) is one of the major greenhouse gases, with a global warming potential about 20 times that of $CO_2$ [1]. As a result, the catalytically complete oxidation of low-concentration methane to $CO_2$ is highly desirable, particularly for the unburned $CH_4$ from natural gas vehicles (NGVs) [2]. NGV exhaust features high throughput, a large amount of water vapor (10–15 %), and high transient temperatures [3–5]. Under such harsh conditions, the methane oxidation catalysts utilized should possess long-term stability under wet conditions and high hydrothermal stability. Among the catalysts developed for methane oxidation, palladium oxide ($PdO_x$) is regarded as the most commonly used active component [6–8], and considerable progress has been achieved in the synthesis of Pd-based catalysts by regulating the Pd species and grain size [9–11], metal−support interactions [12–15], and doping with a second metal [16–18]. However, it is still challenging to achieve the synchronous improvement of hydrothermal stability and long-term stability under conditions of high steam content. During methane oxidation under wet conditions, the generation of inactive $Pd(OH)_2$ sites is usually a critical drawback of Pd-based catalysts, leading to poor long-term stability [19–24]. To combat such loss of long-term stability induced by water vapor, Pt is one of the efficient promoters for Pd-based catalysts [19,25–30]. Under oxidizing conditions, unfortunately, Pt–Pd bimetallic catalysts have usually shown poor hydrothermal stability due to the sintering of Pt–Pd species via Ostwald ripening [31,32]. To suppress the growth of Pt–Pd nanoparticles under hydrothermal conditions, creating anchor sites on the catalyst support would be an effective strategy for designing an all-in-one methane oxidation catalyst for use in NGV exhaust purification. La-loaded γ-$Al_2O_3$ has been widely used as a three-way catalyst (TWC) support [33,34]. It is thought that the loading of La inhibits the sintering and phase transformation of γ-$Al_2O_3$, thus further stabilizing the noble metal active sites [35]. Much attention has been paid to the origins of the high thermostability of La-loaded γ-$Al_2O_3$ [36,37]. However, the direct interaction between La and noble metal

* Corresponding authors at: State Key Joint Laboratory of Environment Simulation and Pollution Control, Research Center for Eco-Environmental Sciences, Chinese Academy of Sciences, Beijing 100085, China.
*E-mail addresses:* ybyu@rcees.ac.cn (Y. Yu), honghe@rcees.ac.cn (H. He).

https://doi.org/10.1016/j.apcatb.2022.122259
Received 19 July 2022; Received in revised form 1 December 2022; Accepted 2 December 2022
Available online 5 December 2022

sites has often been ignored, and it is significant to study and reveal the anchoring effect of La sites for noble metals.

Inspired by the above considerations, herein, we report a PtPd-$La_1$/$Al_2O_3$ catalyst with highly dispersed La sites (denoted as $La_1$) anchoring Pt-doped PdO nanoparticles (NPs) using γ-$Al_2O_3$ support, which exhibited significantly enhanced hydrothermal stability and superior long-term stability under the conditions of simulated NGV exhaust (under a high WHSV of 300,000 mL $g_{cat.}^{-1}$ $h^{-1}$ containing 10 vol% $H_2O$). Detailed studies revealed that Pt-PdO nanoparticles (NPs) were anchored by $La_1$ through electron transfer from $La_1$ to PdO, thus inhibiting the sintering of Pd species during hydrothermal aging. Pt uniformly doped in PdO created high-efficiency Pt sites and unsaturated Pd sites (as well as Pd sites adjacent to O defects) for water-resistance, further enhancing long-term stability. The positive effects of $La_1$ anchoring and Pt doping synergistically contributed to the overall performance of PtPd-$La_1$/$Al_2O_3$.

## 2. Experimental section

### 2.1. Catalyst preparation

Synthesis of Pd/$Al_2O_3$ and PtPd/$Al_2O_3$. Before loading noble metals, the boehmite support (SB-1 supplied by SASOL) was pretreated by calcination at 700 °C for 3 h. The obtained support was denoted as $Al_2O_3$-700. Then, both Pd/$Al_2O_3$ (containing 2.0 wt% Pd) and PtPd/$Al_2O_3$ (containing 1.7 wt% Pd and 0.3 wt% Pt) were prepared by a one-step incipient-wetness impregnation method. In detail, a certain amount of aqueous solution with $Pd(NO_3)_2$ and $Pt(NO_3)_2$ (when used) was added to $Al_2O_3$-700 at room temperature, in which the weight of the solution was ~1.05 times that of $Al_2O_3$-700. After stirring with a glass rod, the resulting mixture was sealed and kept under ambient conditions for 6 h. Subsequently, the sample was dried at 120 °C for 2 h followed by calcination at 550 °C for 2 h. The actual loading of Pd, Pt, and La was analyzed by ICP and listed in Table S1.

Synthesis of Pd-$La_1$/$Al_2O_3$ and PtPd-$La_1$/$Al_2O_3$. Before loading noble metals, 2.0 wt% La was preloaded on $Al_2O_3$-700 by the incipient-wetness impregnation method. In detail, a certain amount of aqueous solution with $La(NO_3)_3$ was added to $Al_2O_3$-700 at room temperature, in which the weight of the solution was ~1.05 times that of $Al_2O_3$-700. After stirring with a glass rod, the resulting mixture was sealed and kept under ambient conditions for 6 h. Subsequently, the intermediate sample was dried at 120 °C for 2 h followed by calcination at 700 °C for 3 h and was denoted as $La_1$/$Al_2O_3$-700. Then, both Pd-$La_1$/$Al_2O_3$ (containing 2.0 wt% Pd) and PtPd-$La_1$/$Al_2O_3$ (containing 1.7 wt% Pd and 0.3 wt % Pt) were prepared by the one-step incipient-wetness impregnation method using $La_1$/$Al_2O_3$-700 as support, the same method as that used for Pd/$Al_2O_3$ and PtPd/$Al_2O_3$. The actual loading of Pd, Pt, and La was analyzed by ICP and listed in Table S1.

Synthesis of PtPd-$La_1$/$Al_2O_3$-800. The synthesis method for PtPd-$La_1$/$Al_2O_3$-800 was almost the same as that for PtPd-$La_1$/$Al_2O_3$, except that the calcination temperatures of boehmite and La-loaded $Al_2O_3$ were changed from 700 ℃ to 800 ℃. It is worth noting that PtPd-$La_1$/$Al_2O_3$-800 was an optimized catalyst. The related data for PtPd-$La_1$/$Al_2O_3$-800 were limited to the activity data shown in Fig. S10.

Hydrothermal aging of catalysts. All the aged catalysts were treated under 10 vol% $H_2O$, 3.5% $O_2$, balanced with $N_2$ at 650 °C for 20 h.

### 2.2. Catalyst evaluation

The methane oxidation tests were conducted in a conventional fixed-bed reactor at atmospheric pressure using a quartz reactor with an inner diameter of 6 mm. Before each test, the catalyst was ground and sieved to 40–60 mesh, then placed in the middle of the quartz reactor without diluent. The light-off curves were tested under a simulated NGVs exhaust comprised of 1000 ppm $CH_4$, 3.5 % $O_2$, 10 vol% $H_2O$, 1000 ppm NO, 6 % $CO_2$, and balanced with $N_2$ under a total flow of 1000 mL $min^{-1}$. 200 mg of catalyst was used in each test, corresponding to a high WHSV of 300,000 mL $g_{cat.}^{-1}$ $h^{-1}$. The catalyst was heated to the desired reaction temperature at a rate of 5 °C $min^{-1}$. Long-term stability tests were performed under the same gas conditions at a constant temperature of 450 °C. The actual temperatures of the catalyst bed were used to plot the activity curves, and the effect of catalyst dilution conditions was evaluated by physically mixing 0.2 g catalyst with 0–0.8 g quartz sand (Fig. S1a). The effect of mass transport was eliminated by using samples with a particle size of 40–60 mesh, which was confirmed by corresponding experiments (Fig. S1b). The methane concentration was analyzed online by an FTIR spectrometer (Nicolet iS10, Thermo Fisher). The conversion ($X$), reaction rate ($r$) and turnover frequency (TOF) of $CH_4$ were calculated as follows:

$$X = \left(1 - \frac{[CH_4]_{out}}{[CH_4]_{in}}\right) \times 100\% \quad (1)$$

$$r = \frac{Q \times X}{V_m \times m_{(Pd+Pt)}} \quad (2)$$

$$TOF = \frac{Q \times X}{V_m \times n_{(Pd+Pt)} \times D_{(Pd+Pt)}} \quad (3)$$

where $[CH_4]_{in}$ and $[CH_4]_{out}$ represent the inlet and outlet concentrations of $CH_4$, respectively. $Q$ represents the flow rate of $CH_4$. $V_m$ represents the molar volume of gas. $n_{(Pd+Pt)}$ represents the total molar amount of Pd and Pt. $m_{(Pd+Pt)}$ represents the total mass of Pd and Pt. $D_{(Pd+Pt)}$ represents the metal dispersion.

## 3. Results and discussion

### 3.1. Characterization of the microstructure of catalysts

The crystal structures of Pd species and $Al_2O_3$ were characterized by X-ray diffraction (XRD) measurements (Fig. 1a). For the Pd/$Al_2O_3$, PtPd/$Al_2O_3$, Pd-$La_1$/$Al_2O_3$, and PtPd-$La_1$/$Al_2O_3$ samples, all the diffraction peaks were assigned to γ-$Al_2O_3$ (PDF: 00-002-1420) and PdO (PDF: 00-043-1024) without peaks assignable to La phases, revealing its uniform dispersion on γ-$Al_2O_3$ [38]. For the La-containing samples, the decreased intensity of the diffraction peaks of the PdO phase indicates a higher degree of dispersion of PdO (or Pt–PdO) than for the La-free ones. $X$-ray absorption spectroscopy (XAS) measurements of Pd K-edge were performed to study the structure of the Pt-$PdO_x$ species (the chi(k) data were shown in Fig. S2). For all four catalysts, the white lines of the $X$-ray absorption near edge structure (XANES) spectra (Fig. 1b) are highly consistent with that of standard PdO. The oxidation state of Pd was further confirmed by the Fourier-transformed extended X-ray absorption fine structure (FT-EXAFS) spectra (Fig. 1c), showing the typical Pd–O and Pd–Pd scatterings of PdO without Pd-Pd scattering from metallic Pd. Qualitatively, the two maxima at around (6.0 $Å^{-1}$, 1.6 Å) and (8.0 $Å^{-1}$, 3.0 Å) in the wavelet transform (WT) plots (Fig. 1d) were assigned to the Pd–O and Pd–Pd scattering signals of PdO, respectively. An increased $k$ value in the second maximum of the Pt-doped sample could be attributed to the overlap of Pd–Pt scattering, corresponding to the doping of Pt into PdO [39,40]. It is noted that although Pt is known to promote the reduction of PdO to metallic Pd [41], in our case, metallic Pd was not found in the fresh catalysts, which might be attributed to the lower Pt/Pd molar ratio (~0.1).

As for the PtPd-$La_1$/$Al_2O_3$ sample, the XAS measurements of Pt $L_3$-edge were performed to study the coordination of Pt (the chi(k) spectra were shown in Fig. S3). The white line intensity of Pt $L_3$-edge XANES spectra (Fig. 2a) was located between that of standard $PtO_2$ and Pt foil, indicating Pt could exist in an oxidation state [53]. The Pt FT-EXAFS spectrum at the Pt $L_3$-edge was compared with that of standard $PtO_2$ and Pt foil, and then the Pd spectrum at the Pd K-edge of standard PdO (Fig. 2b). It can be seen that the coordination of Pt in PtPd-$La_1$/$Al_2O_3$

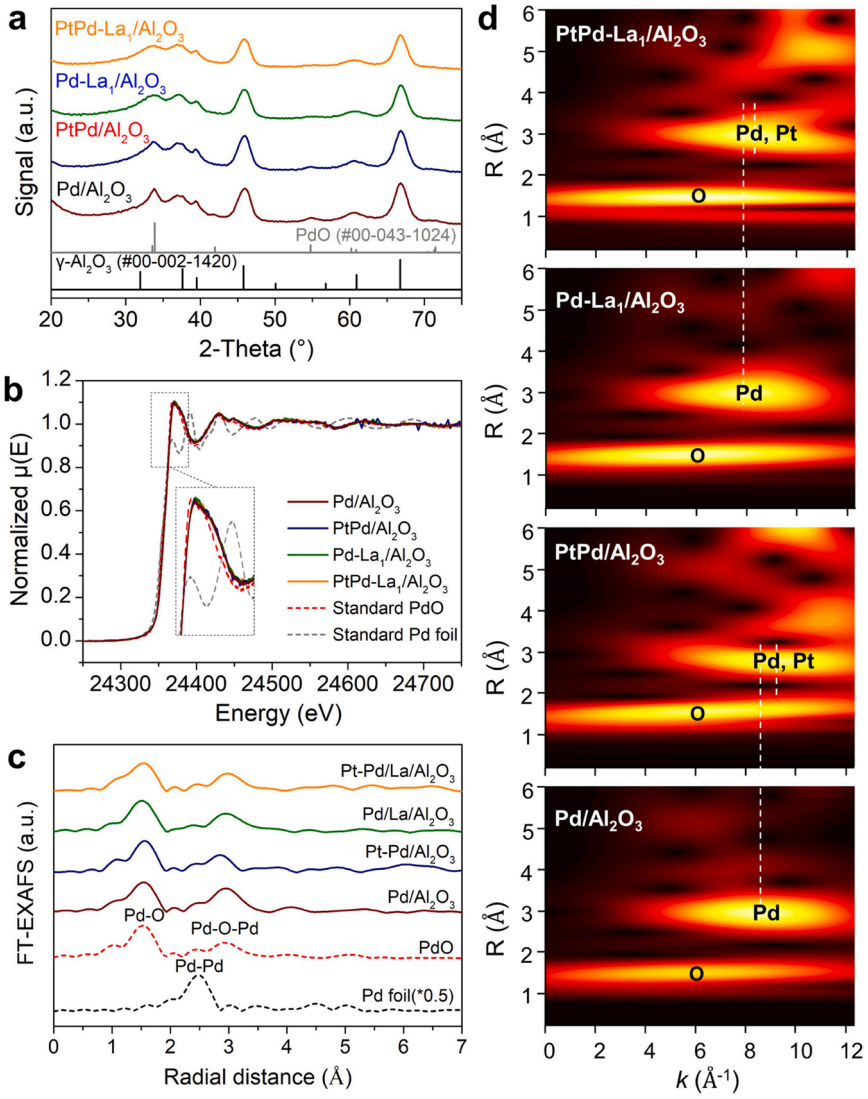


**Fig. 1.** (a) XRD patterns, (b) XANES spectra, (c) $k^2$-weighted FT-EXAFS spectra, and (d) WT plots at the Pd *K*-edge for $Pd/Al_2O_3$, $PtPd/Al_2O_3$, $Pd\text{-}La_1/Al_2O_3$, and $PtPd\text{-}La_1/Al_2O_3$.

was similar to that of Pd in standard PdO. Further fitting analyses (Fig. S4 and Table S2) using the Pt-doped PdO model showed that the main peaks at 1.60 Å, 2.54 Å, and 3.10 Å originated from Pt–O, Pt–Pd, and Pt–O scatterings, respectively. Combining the aberration-corrected high-angle annular dark-field STEM (HAADF-STEM) image and energy-dispersive X-ray (EDX) elemental mapping images (Fig. 2d), the uniform doping of Pt in PdO nanoparticles (NPs) by substituting on Pd sites was confirmed. Additionally, La, Al, and O elements were homogeneously distributed, indicating that La is dispersed evenly on the $Al_2O_3$ support. It should be noted that abundant single-atoms were found in the aberration-corrected HRTEM images of $PtPd\text{-}La_1/Al_2O_3$ (Fig. 2c) and $La_1/Al_2O_3$ (Fig. S5), indicating that La species existed as highly dispersed La sites ($La_1$). This self-dispersion effect of single-atom La on $\gamma\text{-}Al_2O_3$ had been reported by the works of Borisevich et al. and Zhang et al., which was considered to be attributed to the strong adsorption of La atoms on $\gamma\text{-}Al_2O_3$ surfaces and the mutual repulsion among La atoms [51,52]. Glazoff revealed that the absence of the La atoms in the second coordination sphere favored the monoatomic distribution of La atoms on γ-alumina, and the substantial change in the local coordination of the La atoms took place only upon heating up to 1400 °C [54]. To research the changes of La coordination after loading noble metal, the XAS measurements of La $L_3$-edge were performed over $La_1/Al_2O_3$, $Pd\text{-}La_1/Al_2O_3$, and $PtPd\text{-}La_1/Al_2O_3$ samples (Fig. S6). As shown in Fig. S6c, the FT-EXAFS spectrum for $La_1/Al_2O_3$ at the La $L_3$-edge was dominated by the peak of the first shell (around 2 Å), which could be assigned to La–O scattering [51]. With the further loading of noble metals, the scattering intensities of the second shell (3–4 Å) were enhanced in the FT-EXAFS spectra of $PtPd\text{-}La_1/Al_2O_3$ and $Pd\text{-}La_1/Al_2O_3$ samples. However, it was hard to rule out the influence of the accuracy in La EXAFS measurement, because the distance between the La $L_3$-edge and La $L_2$-edge was only ~400 eV [54]. Thus, the interaction between La species and the loaded PdO (or Pt-doped PdO) nanoparticles should be further judged by combining with other characterizations.

### 3.2. *Methane oxidation performance of catalysts*

The catalytic activity of the four above-mentioned samples for methane oxidation was evaluated under simulated NGV exhaust with a high WHSV of 300,000 mL $g_{cat.}^{-1}$ $h^{-1}$ containing 10 vol% $H_2O$. The light-off curves (Fig. 3a) showed that either Pt doping or $La_1$ anchoring reduced the light-off temperatures of methane combustion, and $PtPd\text{-}La_1/Al_2O_3$ showed the lowest $T_{50}$ (light-off temperature for 50 % $CH_4$ conversion) of 395 °C. To reveal the effects of La modification and Pt doping on the intrinsic activity of PdO active sites, the TOFs of the four

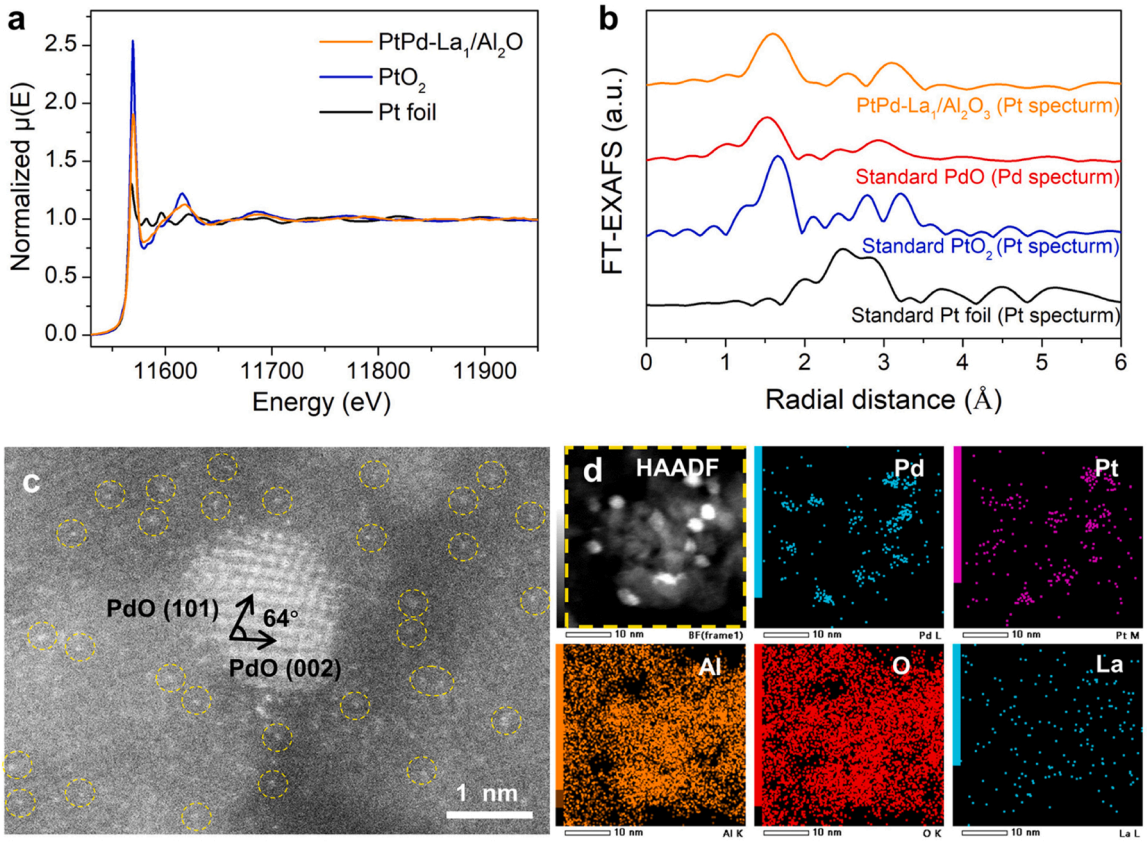


**Fig. 2.** (a) Pt $L_3$-edge XANES spectra, (b) $k^2$-weighted FT-EXAFS spectra at the Pt $L_3$-edge for PtPd-La$_1$/Al$_2$O$_3$, standard PtO$_2$ and Pt foil, and $k^2$-weighted FT-EXAFS spectrum at the Pd K-edge of standard PdO, (c) aberration-corrected HRTEM image and (d) HAADF-STEM and EDS elemental mapping images of PtPd-La$_1$/Al$_2$O$_3$.

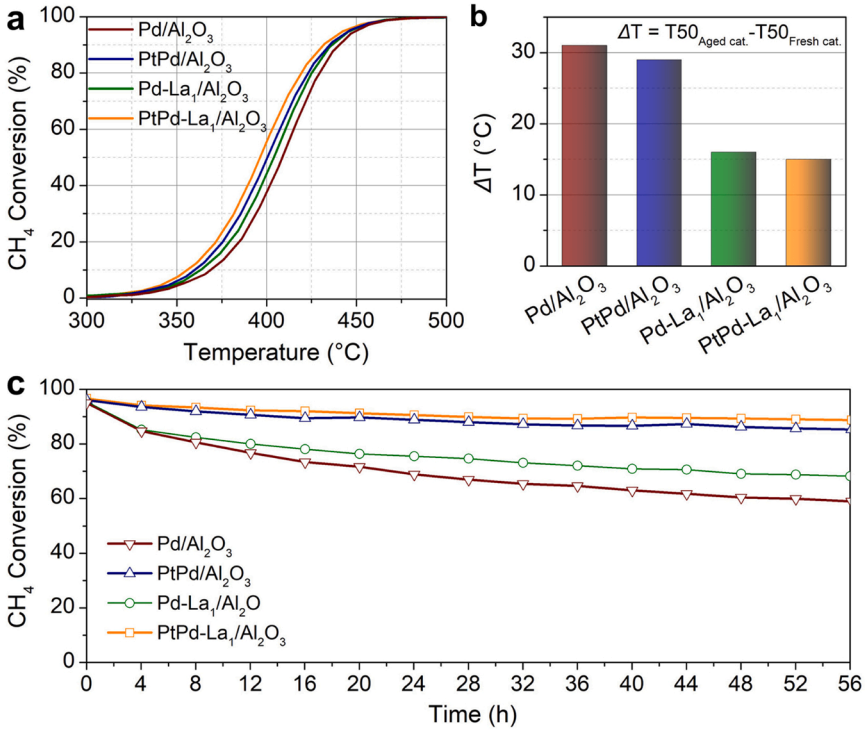


**Fig. 3.** (a) Light-off and (c) long-term stability curves (450 °C for 56 h) of fresh catalysts for methane oxidation, and (b) $T_{50}$ (light-off temperature for 50 % $CH_4$ conversion) differences between aged and fresh catalysts. Test conditions: 1000 ppm $CH_4$, 3.5 % $O_2$, 10 vol% $H_2O$, 1000 ppm NO, 6 % $CO_2$, balanced with $N_2$, WHSV = 300,000 mL $g_{cat.}^{-1}$ $h^{-1}$. Aging conditions: 3.5 % $O_2$, 10 vol% $H_2O$, 650 °C for 20 h. Catalysts: Pd/Al$_2$O$_3$ (Wine), PtPd/Al$_2$O$_3$ (Navy), Pd-La$_1$/Al$_2$O$_3$ (Olive) and PtPd-La$_1$/Al$_2$O$_3$ (Orange).

**Table 1**
Reaction rate and turnover frequency (TOF) of catalysts (370 °C).

| Samples | Reaction rate, μmol• $g^{-1}_{Pd+Pt}$• $sec^{-1}$ | Turnover frequency (TOF), $sec^{-1}$ |
|---|---|---|
| PdPt-$La_1$/$Al_2O_3$ | 35 | 0.0085 |
| Pd-$La_1$/$Al_2O_3$ | 25 | 0.0061 |
| PdPt/$Al_2O_3$ | 30 | 0.0105 |
| Pd/$Al_2O_3$ | 20 | 0.0076 |

catalysts at 370 °C (methane conversion in the range of 5–20 %) were measured and compared with the literature (Table S3). As listed in Table 1, the Pt doping enhanced the intrinsic activity of PdO sites, whereas modification by La reduced the intrinsic activity. Thus, it is worth noting that the reduction of the light-off temperatures by La modification (Fig. 3a) can be attributed to the combined effects of increasing the number of active sites and reducing the intrinsic activity. After aging the samples under hydrothermal conditions, the activities of all the samples deteriorated (Fig. S7), while the La-containing samples exhibited much higher hydrothermal stability when comparing the $T_{50}$ differences between the aged and fresh catalysts (Fig. 3b). It was considered that the loading of La could inhibit the phase transformation and sintering of γ-$Al_2O_3$, thus improving the stability of the catalysts [35]. As shown in Fig. S8, however, no peaks assignable to δ-$Al_2O_3$ or α-$Al_2O_3$ were observed for the fresh and aged catalysts, indicating that the phase transformation of γ-$Al_2O_3$ did not occur. As listed in Table S4, meanwhile, the BET-specific surface areas ($S_{BET}$) of all four catalysts decreased after hydrothermal aging, indicating that sintering of γ-$Al_2O_3$ occurred, but the extent of decrease was consistent (from ~185 $m^2$ $g^{-1}$ to ~165 $m^2$ $g^{-1}$). Thus, after hydrothermal aging, the small decrease in catalytic activity of the La-containing samples could be attributed to γ-$Al_2O_3$ sintering, not the phase transformation of γ-$Al_2O_3$. Additionally, restructuring and de-alloying of Pt-Pd alloys have been reported in previous works [42,43]. However, as shown in the aberration-corrected HRTEM, HAADF-STEM, and EDS elemental mapping images of the hydrothermally aged PtPd/$Al_2O_3$ and PtPd-$La_1$/$Al_2O_3$ in Fig. S9, the Pt-Pd separation phenomenon was not found, which might be attributed to the low Pt/Pd molar ratio (~1:10) of the Pt-containing catalysts in this study. These results indicate that there are other factors governing the improved hydrothermal stability of La-containing samples, such as the direct interaction between $La_1$ and PdO (or Pt-PdO) NPs. The above

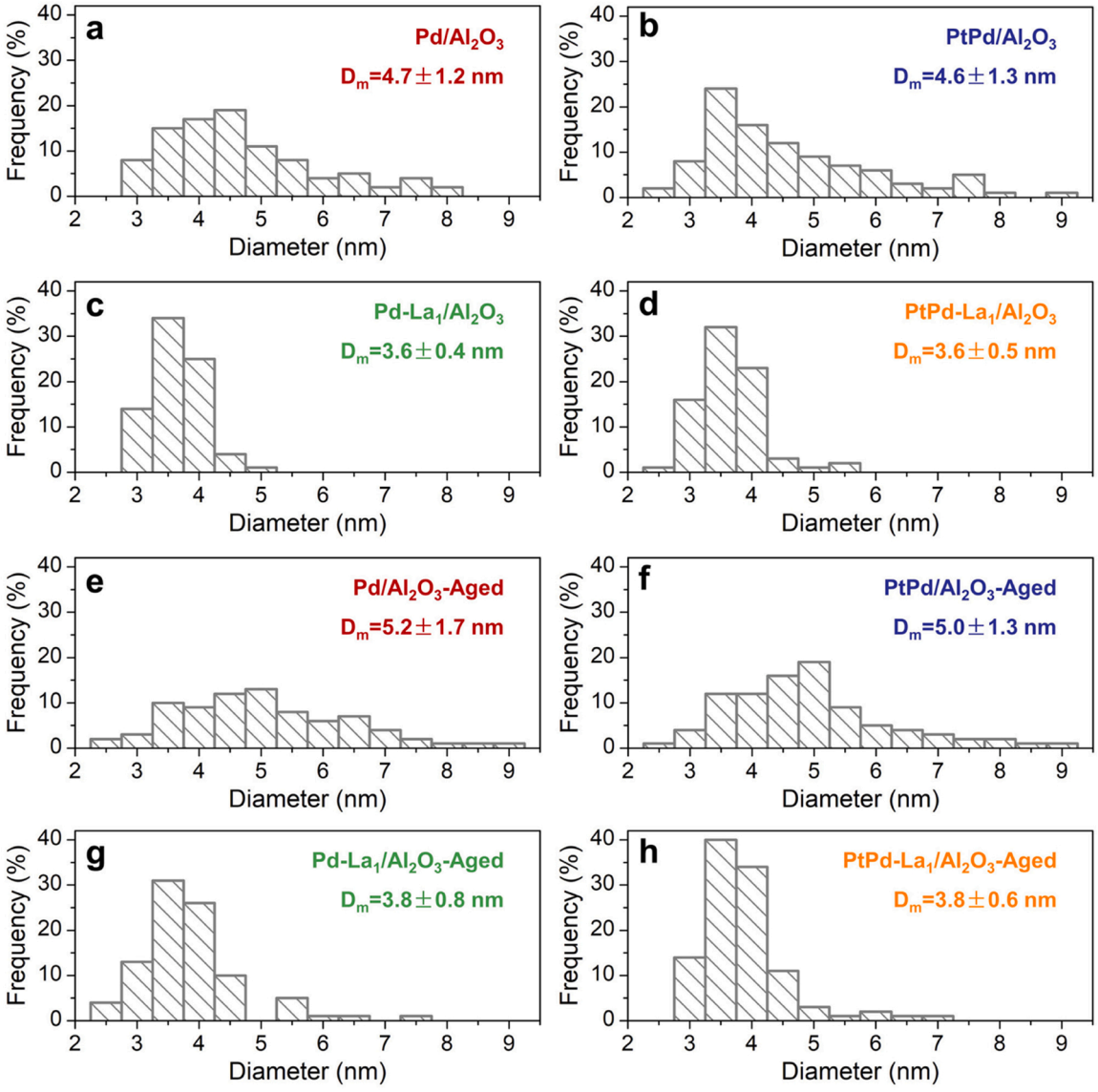


**Fig. 4.** The size distribution of Pd oxide NPs in fresh and aged catalysts. (a) Pd/$Al_2O_3$, (b) PtPd/$Al_2O_3$, (c) Pd-$La_1$/$Al_2O_3$, (d) PtPd-$La_1$/$Al_2O_3$, (e) Pd/$Al_2O_3$-Aged, (f) PtPd/$Al_2O_3$-Aged, (g) Pd-$La_1$/$Al_2O_3$-Aged, and (h) PtPd-$La_1$/$Al_2O_3$-Aged.

results inspired us to improve the thermostability of the γ-$Al_2O_3$ support by increasing the calcination temperature of boehmite from 700 °C to 800 °C, followed by synthesis of the PtPd-$La_1$/$Al_2O_3$-800 sample. Interestingly, the PtPd-$La_1$/$Al_2O_3$-800 sample exhibited remarkable hydrothermal stability without activity loss after aging at 650 °C for 20 h (Fig. S10), confirming the crucial anchoring effect of $La_1$ for PdO (or Pt–PdO) NPs. The long-term stability is also an important criterion for methane oxidation performance in practical applications, which can reveal the water-resistance of catalysts. After reacting at 450 °C for 56 h (Fig. 3c), the $CH_4$ conversion over Pt-free samples dropped significantly, while such deterioration in activity was hardly observed over Pt-doped samples. Among all the samples, PtPd-$La_1$/$Al_2O_3$ showed the best long-term stability, and could maintain ~90 % methane conversion under the harsh simulated NGV conditions. The positive role of Pt doping on long-term stability under wet conditions is consistent with the literature [19,25–30]. And the above results demonstrated that the anchoring effect of $La_1$ sites for Pt-doped PdO NPs does not affect the improvement of water-resistance of PtPd-$La_1$/$Al_2O_3$ due to Pt doing.

### 3.3. Correlations between the methane oxidation performance and the physical and chemical properties of catalysts

To reveal the anchoring effect of $La_1$ for PdO (or Pt-PdO) NPs, the size distributions (Fig. 4) of PdO (or Pt-PdO) NPs were determined for the fresh and aged catalysts based on HRTEM images (Fig. S11 and Fig. S12). For the fresh samples, thoes containing La showed a more centralized size distribution and smaller average sizes for PdO (or Pt-PdO) NPs than the La-free ones. This is consistent with the higher metal dispersion (Table S1) and weaker diffraction peak intensities of PdO in the XRD results of La-containing samples, confirming the anchoring effect of $La_1$. After aging, furthermore, the increase in the average sizes of PdO (or Pt-PdO) NPs was more pronounced over the La-free sample than over the La-doped one, and an apparent sintering phenomenon was also exhibited as revealed by the HRTEM images (Fig. S13). These results, in turn, confirmed the efficient anchoring of Pd oxide by $La_1$, not only facilitating the formation of small-sized Pd species but also inhibiting the sintering of Pd species under hydrothermal conditions.

The chemical properties of Pd species were further investigated through temperature-programmed oxidation (TPO) and temperature-programmed reduction ($H_2$-TPR) measurements. During the heating ramp of the TPO measurements (Fig. 5 a), $O_2$-release peaks for all the samples appeared in the range of 650–850 °C, attributed to the decomposition of Pd oxides. Over the $La_1$-containing sample, only one $O_2$-release peak was found due to the uniform and small size of PdO (or Pt–PdO) NPs. As for the $La_1$-containing samples, the decomposition peaks of PdO species appeared at higher temperatures, indicative of stronger Pd–O bonds due to the interaction between $La_1$ and Pd species. It has been reported that the catalytic oxidation of methane on PdO follows the Mars-van-Krevelen mechanism [4,44]. Thus, the strengthened Pd–O bonds could inhibit the production of O vacancies, leading to the lower intrinsic activity caused by $La_1$ modification (Table 1). Meanwhile, the decomposition temperatures of Pt-doped PdO NPs were lower than the corresponding Pt-free ones, indicating that the Pd–O bonds were weakened by Pt doping, which could explain the higher intrinsic activity of the Pt-doped samples (Table 1). During cooling in the TPO measurements, the re-oxidation peaks of Pd species for all the samples occurred in the low-temperature range of 400–500 °C. This hysteresis indicates that if the samples were reduced by methane in the range of 500–650 °C, Pd (or Pt-Pd) NPs could maintain a reduced state even in $O_2$-containing conditions. These results indicate that from the light-off temperature (~350 °C) to ~500 °C, PdO (or Pt-PdO) NPs are

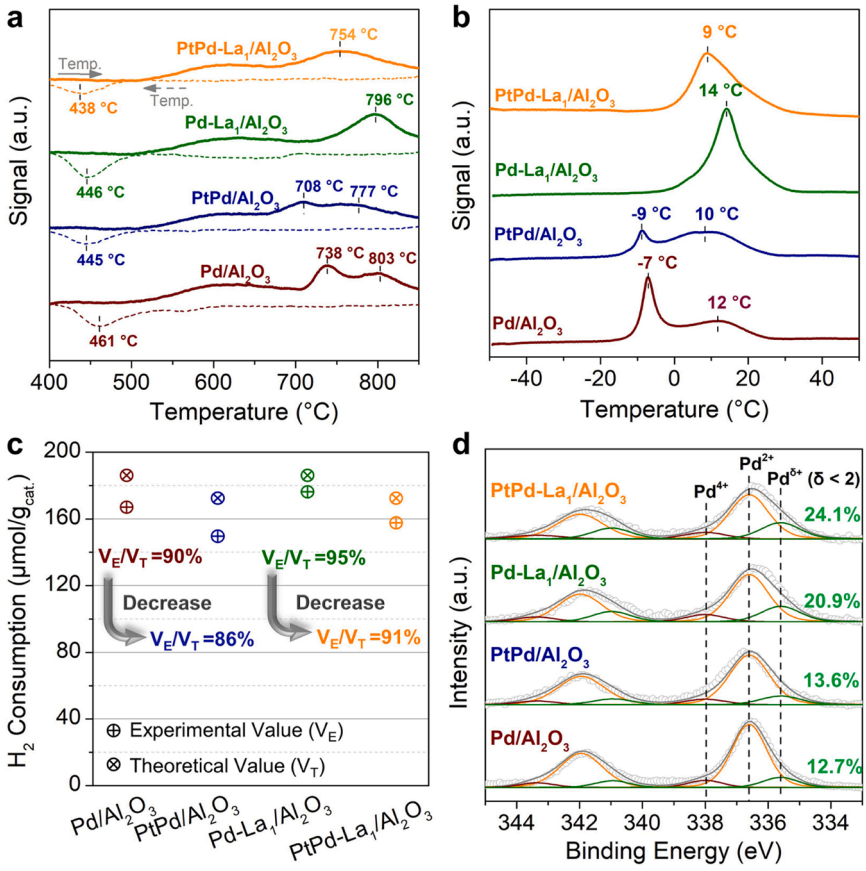


**Fig. 5.** (a) TPO profiles, (b) $H_2$-TPR profiles and (c) corresponding $H_2$ consumptions, and (d) Pd 3*d* photoelectron spectra of samples.

the primary active component for methane oxidation. From the $H_2$-TPR profiles (Fig. 5b) of $La_1$-containing samples, similar to the TPO profiles in the heating ramp, the reduction peaks of Pd oxides were more centralized and appeared at a higher temperature, further confirming the interaction between $La_1$ and Pd species. Based on $H_2$-TPR profiles, the experimental value of $H_2$ consumption (denoted as $V_E$) can be obtained. On the other hand, the uniform active phase of PdO (or Pt-doping PdO) NPs without metallic Pd (or metallic Pt–Pd) was confirmed by the XAFS and EDS elemental results in Section 3.1. Based on the assumption that PdO (or Pt-doping PdO) is a defect-free crystal, the theoretical $H_2$ consumption (denoted as $V_T$) required to reduce this defect-free crystal can be calculated. Thus, the value of $V_E/V_T$ can be used to reflect the relative content of oxygen defects in PdO (or Pt-doping PdO) NPs. As shown in Fig. 5c, the Pt-doped samples showed a lower $V_E/V_T$ ratio than the corresponding Pt-free ones, revealing that Pt doping facilitated the production of oxygen defects in PdO. The surface chemical states of PdO (or Pt-PdO) NPs were further characterized by X-ray photoelectron spectroscopy (XPS) measurements (Fig. 5d). The Pd 3*d* spectra were fitted to the peaks of $Pd^{4+}$ (338.0 eV), $Pd^{2+}$ (336.6 eV), and $Pd^{\delta+}$ ($\delta < 2$) (335.6 eV) according to the literature [4,19,45], among which $Pd^{2+}$ was the main component, corresponding to the Pd species in PdO. The remarkably high content of $Pd^{\delta+}$ ($\delta < 2$) in the La-containing samples further confirmed the strong interaction between $La_1$ and PdO (or Pt-PdO) NPs, probability attributable to the electron transfer from $La_1$ to Pd species. In addition, it could be seen that the content of $Pd^{\delta+}$ ($\delta < 2$) in the Pt-doped samples was higher than the corresponding Pt-free ones. This result further indicated that doping with Pt facilitated the generation of O defects in PdO. Previous studies reported that the addition of Pt tended to create metal sites, whereas Pd favored the formation of metal oxide sites [46,47]. This is similar to the phenomenon that Pt doping in PdO promotes the generation of O defects. The difference in the reduction degree might be attributed to the low Pt doping ratio in the Pt-containing catalysts in this work. The structure of the Pt-doped PdO with O defects provided guidance for the following theoretical calculation studies.

### 3.4. Theoretical calculations on the structure-property relationship

Density functional theory (DFT) calculations were performed to reveal the crucial roles of La anchoring and Pt doping in-depth. In this case, three slab models of PdO-NPs/$Al_2O_3$, PdO-NPs/$La_1$-$Al_2O_3$, and Pt-PdO-NPs/$La_1$-$Al_2O_3$ were built and optimized (Figs. S14–S16) to calculate the combining capacity between PdO (or Pt-doped PdO) clusters and the $Al_2O_3$(110) (or $La_1$-$Al_2O_3$(110)) surface. The binding energies (Fig. 6a) of PdO and Pt-PdO on the $La_1$-$Al_2O_3$ surface are − 6.6 eV and − 6.8 eV, respectively, both of which are higher than that of PdO on $Al_2O_3$ (−5.0 eV), confirming the anchoring effect of the $La_1$ site for PdO or Pt-PdO. The planar average differential charge density (z-direction) was also calculated for PdO-NPs/$Al_2O_3$ (Fig. 6d), PdO-NPs/$La_1$-$Al_2O_3$ (Fig. 6e), and Pt-PdO-NPs/$La_1$-$Al_2O_3$ (Fig. 6 f). In these three models, the introduction of $La_1$ sites markedly improved the electron transfer from the support to PdO (or Pt-PdO), with the number of transferred electrons from $La_1$-$Al_2O_3$ to Pt-PdO increasing to 2.39 $e^-$. These findings are consistent with the high content of $Pd^{\delta+}$ ($\delta < 2$) in the La-containing samples in the XPS results. Thus, the anchoring effect of $La_1$ for PdO (or Pt-PdO) can be attributed to the robust capacity for donating electrons from $La_1$ to PdO (or Pt-PdO). Additionally, this electron donation from $La_1$ to PdO (or Pt-PdO) might strengthen the Pd–O bonds, leading to the high decomposition temperatures of Pd oxides and the relatively low intrinsic activity of La-containing samples. To clarify the effect of Pt doping on methane oxidation, slab models of pure PdO(101) (denoted as PdO(101)) and Pt-doped PdO(101) with oxygen defects (denoted as Pt-PdO-$O_v$) were built according to the characterization results. For these models, the energy barrier for breaking the first C–H bond of $CH_4$, which has been proven to be the rate-determining step for methane oxidation [48–50], was firstly computed (Fig. 6b, Fig. S17). On the Pt site of the Pt-PdO-$O_v$ surface, the barrier for C–H bond breaking is 0.56 eV, which is lower than the barrier on the Pd site of PdO (101) (0.71 eV) and is consistent with the previous results [9,19,26]. However, the Pd-$O_v$ site (the Pd site adjacent to the O defect) of the Pt-PdO-$O_v$ surface shows a high barrier of 0.94 eV. Thus, the slight improvement in methane oxidation activity of the Pt-doped samples could be attributed to the combined effect of Pd-$O_v$ and Pt-substituted sites of PdO. Regarding the

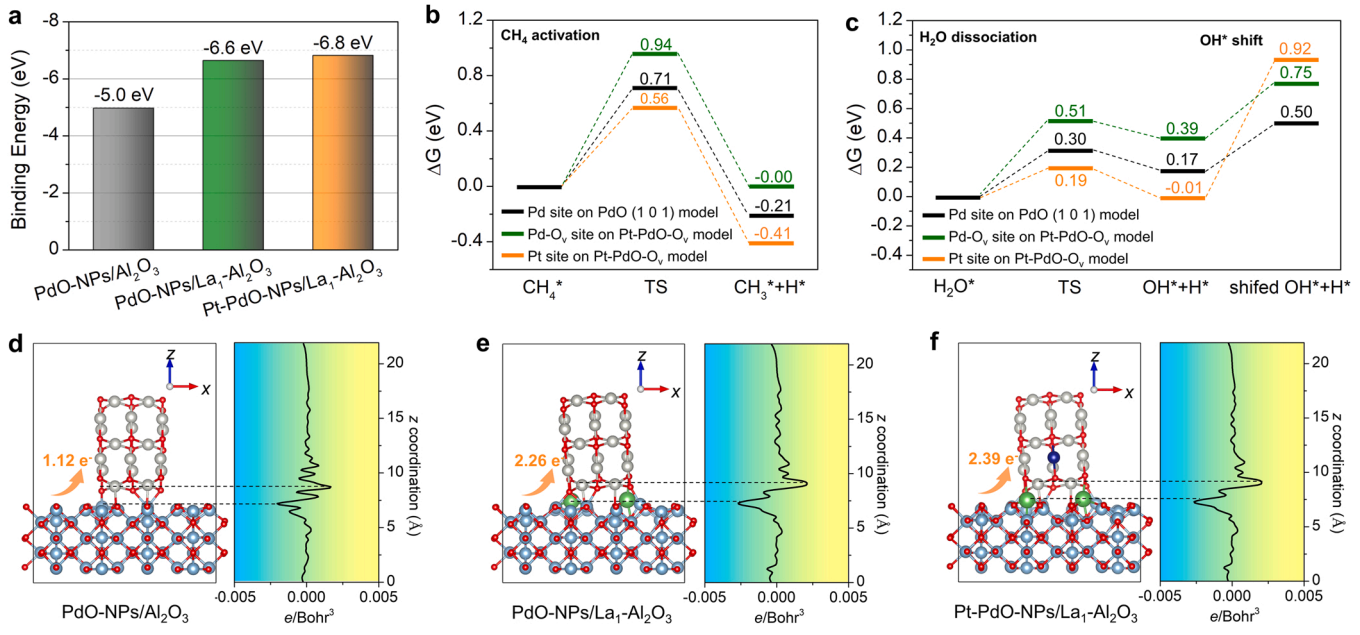


**Fig. 6.** DFT calculations on (a) the cluster binding energy of PdO (or Pt-doped PdO) on $Al_2O_3$ and $La_1$-$Al_2O_3$ surfaces; the side views of the optimized structures and the corresponding planar average differential charge density in the *z*-direction of (d) PdO-NPs/$Al_2O_3$, (e) PdO-NPs/$La_1$-$Al_2O_3$, and (f) Pt-PdO-NPs/$La_1$-$Al_2O_3$. The energy barriers for (b) methane dissociation and (c) water dissociation and the following OH* shift process over the PdO (101) and Pt-PdO-$O_v$ (101) models. The Gibbs free energy values were calculated using a temperature of 450 °C.

water-resistance of Pd-based catalysts for methane oxidation, the generation of Pd hydroxyl species usually leads to a critical drawback of Pd-based catalysts [21,22]. The existence of the equilibrium PdO + $H_2O$ = $Pd(OH)_2$ was reported, where PdO and $Pd(OH)_2$ represented the active phase and inactive surface state for methane oxidation, respectively [23,24]. By using in situ DRIFTS measurements, Zou et al. found that $OH^-$ species formed and accumulated over the surface of Pd-based catalysts during methane oxidation [20]. As predicted by DFT calculations, Xiong et al. reported that the OH* species produced by water dissociation could poison the surface sites of PdO due to the high binding energy of Pd–OH [19]. With these facts in mind, the energy barrier of water dissociation and the following OH* shift processes were further computed to verify the enhancement effect of Pt doping on water resistance (Fig. 6c and Fig. S18). On the Pd site of the PdO (101) model, the energy barriers for water dissociation and the following OH* shift processes are 0.30 eV and 0.33 eV, respectively, indicating that an isolated Pd–OH on the Pd site of the PdO (101) can be easily formed. On the Pt site of the Pt-PdO-$O_v$ (101) model, although chemisorbed OH* and H* can be easily formed with a low barrier of 0.19 eV, the high barrier for the OH* shift (0.93 eV) can inhibit the formation of isolated Pd–OH. On the Pd-$O_v$ site (Pd site adjacent to the O defect) of the Pt-PdO-$O_v$ (101) model, the barrier for water dissociation is up to 0.51 eV. Therefore, both Pt sites and Pd-$O_v$ sites in the Pt-PdO-$O_v$ (101) model are not conducive to the formation of isolated Pd–OH, which could be the reason why the Pt-doped samples showed better water resistance for methane oxidation and long-term stability in the presence of steam.

## 4. Conclusion

In this work, we developed a new catalyst with highly dispersed La sites anchoring Pt-PdO nanoparticles on a lanthanum-loaded aluminum oxide support (PtPd-$La_1/Al_2O_3$) for methane oxidation. Under the harsh conditions of simulated NGV exhaust, PtPd-$La_1/Al_2O_3$ exhibited excellent reactivity, long-term stability, and significantly enhanced hydrothermal stability. The structure-property relationship was also revealed by a series of characterization techniques, including XPS, XAFS, HAADF-STEM, and DFT calculations. Pt uniformly doped in PdO created high-efficiency Pt sites and unsaturated Pd sites (as well as Pd sites adjacent to O defects) for water-resistance, further enhancing long-term stability. $La_1$ sites played a crucial role in anchoring Pt-PdO nanoparticles (NPs) due to the electron transfer from the $La_1$-$Al_2O_3$ support to Pd oxide NPs. The anchoring effect of $La_1$ contributed to the high dispersion of Pt-Pd species and the significant hydrothermal stability of the catalyst. This work developed an all-in-one catalyst for methane oxidation and provided molecular-level insights into the chemical and physical stability of active palladium sites.

## CRediT authorship contribution statement

**Z. Liu:** Conceptualization, Data curation, Formal analysis, Investigation, DFT calculation, Writing – original draft. **G. Xu:** Formal analysis. **L. Zeng:** Data curation, Formal analysis. **W. Shi:** Formal analysis. **Y. Wang:** Formal analysis. **Y. Sun:** Formal analysis. **Y. Yun:** Conceptualization, Supervision, Writing – review & editing, Funding acquisition. **H. Hong:** Conceptualization, Supervision, Writing – review & editing, Funding acquisition.

## Declaration of Competing Interest

The authors declare that they have no known competing financial interests or personal relationships that could have appeared to influence the work reported in this paper.

## Data availability

Data will be made available on request.

## Acknowledgement

This work was supported by National Natural Science Foundation of China (U20B6004, 22106172, and 22072179), China Postdoctoral Science Foundation (2021M703409), and Special Project of Eco-environmental Technology for Peak Carbon Dioxide Emissions and Carbon Neutrality (RCEES-TDZ-2021-2).

## Appendix A. Supporting information

Supplementary data associated with this article can be found in the online version at doi:10.1016/j.apcatb.2022.122259.

## References

[1] M. Cargnello, J.J.D. Jaén, J.C.H. Garrido, K. Bakhmutsky, T. Montini, J.J.C. Gámez, R.J. Gorte, P. Fornasiero, Exceptional activity for methane combustion over modular Pd@$CeO_2$ subunits on functionalized $Al_2O_3$, Science 337 (2012) 713–717, https://doi.org/10.1126/science.1222887.
[2] J. Xiong, J. Yang, X. Chi, K. Wu, L. Song, T. Li, Y. Zhao, H. Huang, P. Chen, J. Wu, L. Chen, M. Fu, D. Ye, Pd-promoted $Co_2NiO_4$ with lattice CoONi and interfacial PdO activation for highly efficient methane oxidation, Appl. Catal. B 292 (2021), 120201, https://doi.org/10.1016/j.apcatb.2021.120201.
[3] G. Zhao, X. Pan, Z. Zhang, Y. Liu, Y. Lu, A thin-felt Pd–MgO–$Al_2O_3$/Al-fiber catalyst for catalytic combustion of methane with resistance to water-vapor poisoning, J. Catal. 384 (2020) 122–135, https://doi.org/10.1016/j.jcat.2020.01.013.
[4] J. Yang, M. Peng, G. Ren, H. Qi, X. Zhou, J. Xu, F. Deng, Z. Chen, J. Zhang, K. Liu, X. Pan, W. Liu, Y. Su, W. Li, B. Qiao, D. Ma, T. Zhang, A. Hydrothermally Stable, Irreducible oxide-modified Pd/$MgAl_2O_4$ catalyst for methane combustion, Angew. Chem. Int. Ed. 59 (2020) 18522–18526, https://doi.org/10.1002/anie.202009050.
[5] D. Jiang, K. Khivantsev, Y. Wang, Low-temperature methane oxidation for efficient emission control in natural gas vehicles: Pd and beyond, ACS Catal. 10 (2020) 14304–14314, https://doi.org/10.1021/acscatal.0c03338.
[6] R.J. Farrauto, Low-temperature oxidation of methane, Science 337 (2012) 659–660, https://doi.org/10.1126/science.1226310.
[7] K. Khivantsev, N.R. Jaegers, L. Kovarik, M. Wang, J.Z. Hu, Y. Wang, M. A. Derewinski, J. Szanyi, The superior hydrothermal stability of Pd/SSZ-39 in low temperature passive NOx adsorption (PNA) and methane combustion, Appl. Catal. B 280 (2021), 119449, https://doi.org/10.1016/j.apcatb.2020.119449.
[8] Y. Ding, Q. Wu, B. Lin, Y. Guo, Y. Guo, Y. Wang, L. Wang, W. Zhan, Superior catalytic activity of a Pd catalyst in methane combustion by fine-tuning the phase of ceria-zirconia support, Appl. Catal. B 266 (2020), 118631, https://doi.org/10.1016/j.apcatb.2020.118631.
[9] W. Huang, A.C. Johnston-Peck, T. Wolter, W.-C.D. Yang, L. Xu, J. Oh, B.A. Reeves, C. Zhou, M.E. Holtz, A.A. Herzing, A.M. Lindenberg, M. Mavrikakis, M. Cargnello, Steam-created grain boundaries for methane C–H activation in palladium catalysts, Science 373 (2021) 1518–1523, https://doi.org/10.1126/science.abj5291.
[10] J. Xu, L. Ouyang, W. Mao, X.-J. Yang, X.-C. Xu, J.-J. Su, T.-Z. Zhuang, H. Li, Y.-F. Han, Operando and kinetic study of low-temperature, lean-burn methane combustion over a Pd/γ-$Al_2O_3$ catalyst, ACS Catal. 2 (2012) 261–269, https://doi.org/10.1021/cs200694k.
[11] K. Murata, Y. Mahara, J. Ohyama, Y. Yamamoto, S. Arai, A. Satsuma, The metal–support interaction concerning the particle size effect of Pd/$Al_2O_3$ on methane combustion, Angew. Chem. Int. Ed. 56 (2017) 15993–15997, https://doi.org/10.1002/anie.201709124.
[12] K. Murata, D. Kosuge, J. Ohyama, Y. Mahara, Y. Yamamoto, S. Arai, A. Satsuma, Exploiting metal−support interactions to tune the redox properties of supported Pd catalysts for methane combustion, ACS Catal. 10 (2020) 1381–1387, https://doi.org/10.1021/acscatal.9b04524.
[13] M. Tang, S. Li, S. Chen, Y. Ou, M. Hiroaki, W. Yuan, B. Zhu, H. Yang, Y. Gao, Z. Zhang, Y. Wang, Facet-dependent oxidative strong metal-support interactions of palladium–$TiO_2$ determined by in situ transmission electron microscopy, Angew. Chem. Int. Ed. 60 (2021) 22339–22344, https://doi.org/10.1002/anie.202106805.
[14] A. Toso, S. Colussi, S. Padigapaty, C. d Leitenburg, A. Trovarelli, High stability and activity of solution combustion synthesized Pd-based catalysts for methane combustion in presence of water, Appl. Catal. B 230 (2018), 120201, https://doi.org/10.1016/j.apcatb.2018.02.049.
[15] H. Duan, R. You, S. Xu, Z. Li, K. Qian, T. Cao, W. Huang, X. Bao, Pentacoordinated $Al^{3+}$-stabilized active Pd structures on $Al_2O_3$-coated palladium catalysts for methane combustion, Angew. Chem. Int. Ed. 58 (2019) 12043–12048, https://doi.org/10.1002/anie.201904883.
[16] J.J. Willis, E.D. Goodman, L. Wu, A.R. Riscoe, P. Martins, C.J. Tassone, M. Cargnello, Systematic identification of promoters for methane oxidation catalysts using size- and composition-controlled Pd-based bimetallic nanocrystals, J. Am. Chem. Soc. 139 (2017) 11989–11997, https://doi.org/10.1021/jacs.7b06260.
[17] I. Friberg, N. Sadokhina, L. Olsson, Complete methane oxidation over Ba modified Pd/$Al_2O_3$: the effect of water vapor, Appl. Catal. B 231 (2018) 242–250, https://doi.org/10.1016/j.apcatb.2018.03.003.
[18] C. Chen, Y.-H. Yeh, M. Cargnello, C.B. Murray, P. Fornasiero, R.J. Gorte, Methane oxidation on Pd@$ZrO_2$/Si−$Al_2O_3$ is enhanced by surface reduction of $ZrO_2$, ACS Catal. 4 (2014) 3902–3909, https://doi.org/10.1021/cs501146u.

[19] H. Xiong, D. Kunwar, D. Jiang, C.E. García-Vargas, H. Li, C. Du, G. Canning, X. I. Pereira-Hernandez, Q. Wan, S. Lin, S.C. Purdy, J.T. Miller, K. Leung, S.S. Chou, H.H. Brongersma, R. ter Veen, J. Huang, H. Guo, Y. Wang, A.K. Datye, Engineering catalyst supports to stabilize $PdO_x$ two-dimensional rafts for water-tolerant methane oxidation, Nat. Catal. 4 (2021) 830–839, https://doi.org/10.1038/s41929-021-00680-4.

[20] X. Zou, Z. Rui, S. Song, H. Ji, Enhanced methane combustion performance over $NiAl_2O_4$-interfacepromoted Pd/c-$Al_2O_3$, J. Catal. 338 (2016) 192–201, https://doi.org/10.1016/j.jcat.2015.12.031.

[21] A.W. Petrov, D. Ferri, O. Krӧcher, J.A. v Bokhoven, Design of stable palladium-based zeolite catalysts for complete methane oxidation by postsynthesis zeolite modification, ACS Catal. 9 (2019) 2303–2312, https://doi.org/10.1021/acscatal.8b04486.

[22] X. Zoua, J. Chenb, Z. Ruib, H. Ji, Sequential growth reveals multi-spinel interface promotion for methane combustion over alumina supported palladium catalyst, Appl. Catal. B 273 (2020), 119071, https://doi.org/10.1016/j.apcatb.2020.119071.

[23] P. Gélin, M. Primet, Complete oxidation of methane at low temperature over noble metal based catalysts: a review, Appl. Catal. B 39 (2002) 1–37, https://doi.org/10.1016/S0926-3373(02)00076-0.

[24] R. Burch, F.J. Urbano, P.K. Loader, Methane combustion over palladium catalysts: the effect of carbon dioxide and water on activity, Appl. Catal. A 123 (1995) 173–184, https://doi.org/10.1016/0926-860X(94)00251-7.

[25] E.D. Goodman, S. Dai, A.-C. Yang, C.J. Wrasman, A. Gallo, S.R. Bare, A.S. Hoffman, T.F. Jaramillo, G.W. Graham, X. Pan, M. Cargnello, Uniform Pt/Pd bimetallic nanocrystals demonstrate platinum effect on palladium methane combustion activity and stability, ACS Catal. 7 (2017) 4372–4380, https://doi.org/10.1021/acscatal.7b00393.

[26] P. Castellazzi, G. Groppi, P. Forzatti, Effect of Pt/Pd ratio on catalytic activity and redox behavior of bimetallic Pt–Pd/$Al_2O_3$ catalysts for $CH_4$ combustion, Appl. Catal. B 95 (2010) 303–311, https://doi.org/10.1016/j.apcatb.2010.01.008.

[27] J. Lee, M. Young Kim, J. Hong Jeon, D.H. Lee, K.N. Rao, D.G. Oh, E. Jeong Jang, E. Kim, S.C. Na, H.S. Han, J.H. Kwak, Effect of Pt pre-sintering on the durability of PtPd/$Al_2O_3$ catalysts for $CH_4$ oxidation, Appl. Catal. B 260 (2020), 118098, https://doi.org/10.1016/j.apcatb.2019.118098.

[28] H. Nie, J.Y. Howe, P.T. Lachkov, Y.-H.C. Chin, Chemical and structural dynamics of nanostructures in bimetallic Pt−Pd catalysts, their inhomogeneity, and their roles in methane oxidation, ACS Catal. 9 (2019) 5445–5461, https://doi.org/10.1021/acscatal.9b00485.

[29] J. Park, D. Kim, S.W. Byun, H. Shin, Y. Ju, H. Min, Y.J. Kim, I. Heo, M.J. Hazlett, M. Kim, S.B. Kang, Impact of Pd:Pt ratio of Pd/Pt bimetallic catalyst on $CH_4$ oxidation, Appl. Catal. B 316 (2022), 121623, https://doi.org/10.1016/j.apcatb.2022.121623.

[30] H. Xiong, M.H. Wiebenga, C. Carrillo, J.R. Gaudet, H.N. Pham, D. Kunwar, S.H. Oh, G. Qi, C.H. Kim, A.K. Datye, Design considerations for low-temperature hydrocarbon oxidation reactions on Pd based catalysts, Appl. Catal. B 236 (2018) 436–444, https://doi.org/10.1016/j.apcatb.2018.05.049.

[31] G.W. Graham, H.W. Jen, O. Ezekoye, R.J. Kudla, W. Chun, X.Q. Pan, R.W. McCabe, Effect of alloy composition on dispersion stability and catalytic activity for NO oxidation over alumina-supported Pt–Pd catalysts, Catal. Lett. 116 (2007) 1–8, https://doi.org/10.1007/s10562-007-9124-7.

[32] T.R. Johns, R.S. Goeke, V. Ashbacher, P.C. Thüne, J.W. Niemantsverdriet, B. Kiefer, C.H. Kim, M.P. Balogh, A.K. Datye, Relating adatom emission to improved durability of Pt–Pd diesel oxidation catalysts, J. Catal. 328 (2015) 151–164, https://doi.org/10.1016/j.jcat.2015.03.016.

[33] Y. Jing, Z. Cai, C. Liu, T. Toyao, Z. Maeno, H. Asakura, S. Hiwasa, S. Nagaoka, H. Kondoh, K.-i. Shimizu, Promotional effect of La in the three-way catalysis of La-loaded $Al_2O_3$-supported Pd catalysts (Pd/La/$Al_2O_3$), ACS Catal. 10 (2020) 1010–1023, https://doi.org/10.1021/acscatal.9b03766.

[34] J. Wang, H. Chen, Z. Hu, M. Yao, Y. Li, A review on the Pd-based three-way catalyst, Catal. Rev. 57 (2015) 79–144, https://doi.org/10.1080/01614940.2014.977059.

[35] Y. Yao, R. Fang, Z. Shi, M. Gong, Y. Chen, The effect of $La_2O_3$ on Pd close-coupled catalysts, Chin. J. Catal. 32 (2011) 589–594, https://doi.org/10.1016/S1872-2067(10)60204-5.

[36] S. Wang, A.Y. Borisevich, S.N. Rashkeev, M.V. Glazoff, K. Sohlberg, S. J. Pennycook, S.T. Pantelides, Dopants adsorbed as single atoms prevent degradation of catalysts, Nat. Mater. 3 (2004) 143–146, https://doi.org/10.1038/nmat1077.

[37] T. Yamamoto, T. Hatsui, T. Matsuyama, T. Tanaka, T. Funabiki, Structures and acid-base properties of La/$Al_2O_3$ – role of la addition to enhance thermal stability of γ-$Al_2O_3$, Chem. Mater. 15 (2003) 4830–4840, https://doi.org/10.1021/cm034732c.

[38] K. Murata, J. Ohyama, Y. Yamamoto, S. Arai, A. Satsuma, Methane combustion over Pd/$Al_2O_3$ catalysts in the presence of water: effects of Pd particle size and alumina crystalline phase, ACS Catal. 10 (2020) 8149–8156, https://doi.org/10.1021/acscatal.0c02050.

[39] J. Timoshenko, A. Kuzmin, Wavelet data analysis of EXAFS spectra, Comput. Phys. Commun. 180 (2009) 920–925, https://doi.org/10.1016/j.cpc.2008.12.020.

[40] Z. Liu, G. Sun, C. Chen, K. Sun, L. Zeng, L. Yang, Y. Chen, W. Wang, B. Liu, Y. Lu, Y. Pan, Y. Liu, C. Liu, Fe-doped $Mn_3O_4$ spinel nanoparticles with highly exposed $Fe_{oct}$−O−$Mn_{tet}$ sites for efficient selective catalytic reduction (SCR) of NO with ammonia at low temperatures, ACS Catal. 10 (2020) 6803–6809, https://doi.org/10.1021/acscatal.0c01284.

[41] H. Nassiri, K.-E. Lee, Y. Hu, R.E. Hayes, R.W.J. Scott, N. Semagina, Platinum inhibits low-temperature dry lean methane combustion through palladium reduction in Pd−Pt/$Al_2O_3$: an insitu X-ray absorption study, ChemPhysChem 18 (2017) 238, https://doi.org/10.1002/cphc.201600993.

[42] J. Schütz, H. Störmer, P. Lott, O. Deutschmann, Effects of hydrothermal aging on CO and NO oxidation activity over monometallic and bimetallic Pt-Pd catalysts, Catalysts 11 (2021) 300, https://doi.org/10.3390/catal11030300.

[43] A. Morlang, U. Neuhausen, K.V. Klementiev, F.-W. Schütze, G. Miehe, H. Fuess, E. S. Lox, Bimetallic Pt/Pd diesel oxidation catalysts Structural characterisation and catalytic behaviour, Appl. Catal. B 60 (2005) 191–199, https://doi.org/10.1016/j.apcatb.2005.03.007.

[44] J. Lin, Y. Chen, X. Liu, X. Chen, Y. Zheng, F. Huang, Y. Xiao, Y. Zheng, L. Jiang, Microstructural property regulation and performance in methane combustion reaction of ordered mesoporous alumina supported palladium-cobalt bimetallic catalysts, Appl. Catal. B 263 (2020), 118269, https://doi.org/10.1016/j.apcatb.2019.118269.

[45] R.G. Rao, R. Blume, T.W. Hansen, E. Fuentes, K. Dreyer, S. Moldovan, O. Ersen, D. D. Hibbitts, Y.J. Chabal, R. Schlögl, J.-P. Tessonnier, Interfacial charge distributions in carbon-supported palladium catalysts, Nat. Commun. 8 (2017) 340, https://doi.org/10.1038/s41467-017-00421-x.

[46] H. Xiong, M.H. Wiebenga, C. Carrillo, J.R. Gaudet, H.N. Pham, D. Kunwar, S.H. Oh, G. Qi, C.H. Kim, A.K. Datye, Design considerations for low-temperature hydrocarbon oxidation reactions on Pd based catalysts, Appl. Catal. B 236 (2018) 436–444, https://doi.org/10.1016/j.apcatb.2018.05.049.

[47] N.M. Kinnunen, J.T. Hirvi, M. Suvanto, T.A. Pakkanen, Methane combustion activity of Pd–$PdO_x$–Pt/$Al_2O_3$ catalyst: the role of platinum promoter, J. Mol. Catal. A 356 (2012) 20–28, https://doi.org/10.1016/j.molcata.2011.12.023.

[48] M.V. d Bossche, H. Grönbeck, Methane oxidation over PdO(101) revealed by first-principles kinetic modeling, J. Am. Chem. Soc. 137 (2015) 12035–12044, https://doi.org/10.1021/jacs.5b06069.

[49] M. Jørgensen, H. Grönbeck, First-principles microkinetic modeling of methane oxidation over Pd(100) and Pd(111, ACS Catal. 6 (2016) 6730–6738, https://doi.org/10.1021/acscatal.6b01752.

[50] Y.-H. Chin, C. Buda, M. Neurock, E. Iglesia, Consequences of metal−oxide interconversion for C−H bond activation during $CH_4$ reactions on Pd catalysts, J. Am. Chem. Soc. 135 (2013) 15425–15442, https://doi.org/10.1021/ja405004m.

[51] S. Wang, A. Borisevich, S. Rashkeev, M. Glazoff, K. Sohlberg, S. Pennycook, S. Pantelides, Dopants adsorbed as single atoms prevent degradation of catalysts, Nat. Mater. 3 (2004) 143–146, https://doi.org/10.1038/nmat1077.

[52] X.-F. Yang, A. Wang, B. Qiao, J. Li, J. Liu, T. Zhang, Single-atom catalysts: a new frontier in heterogeneous catalysis, Acc. Chem. Res. 46 (2013) 1740–1748, https://doi.org/10.1021/ar300361m.

[53] K. Sasaki, N. Marinkovic, H.S. Isaacs, R.R. Adzic, Synchrotron-based in situ characterization of carbon-supported platinum and platinum monolayer electrocatalysts, ACS Catal. 6 (2016) 69–76, https://doi.org/10.1021/acscatal.5b01862.

[54] M.V. Glazoff, Synchrotron EXAFS and XANES spectroscopy studies of transition aluminas doped with La and Cr for catalytic applications, Appl. Phys. A 122 (2016) 386, https://doi.org/10.1007/s00339-016-9737-z.